



# Development of intertwined nanostructured multi-phase air electrodes for efficient and durable reversible solid oxide cells

Zhiyi Chen<sup>a,1</sup>, Lizhen Jiang<sup>a,1</sup>, Shuai He<sup>b</sup>, Chengzhi Guan<sup>c</sup>, Yuanfeng Zou<sup>a</sup>, Zhongwei Yue<sup>a</sup>, Na Ai<sup>d</sup>, San Ping Jiang<sup>b,\*</sup>, Yanqun Shao<sup>a</sup>, Kongfa Chen<sup>a,\*</sup>

<sup>a</sup> College of Materials Science and Engineering, Fuzhou University, Fuzhou, Fujian 350108, China

<sup>b</sup> WA School of Mines: Minerals, Energy and Chemical Engineering, Curtin University, Perth, WA 6102, Australia

<sup>c</sup> Key Laboratory of Interfacial Physics and Technology, Shanghai Institute of Applied Physics, Chinese Academy of Sciences, Shanghai 201800, China

<sup>d</sup> Fujian College Association Instrumental Analysis Center, Fuzhou University, Fuzhou, Fujian 350108, China

## ARTICLE INFO

### Keywords:

Reversible solid oxide cells  
Intertwined nanostructured electrodes  
Electrode/electrolyte interface  
Double perovskite  
Multi-phases

## ABSTRACT

The development of nanostructured electrodes of solid oxide cells is largely hindered by the high temperature sintering process and limited in the loading and choices of catalytic phases. Here, a nanostructured multi-phase air electrode is fabricated via facile combination of  $\text{Gd}_{0.2}\text{Ce}_{0.8}\text{O}_{1.9}$  (GDC) decorated  $\text{PrBa}_{0.8}\text{Ca}_{0.2}\text{Co}_2\text{O}_{5+\delta}$  (PBCC) and direct assembly approach. The highly flexible decoration process and the in situ formation of multi-phases lead to the formation of intertwined core-shell type nanostructures with intimate electrode/electrolyte interface. A cell with a 40 wt% GDC decorated PBCC electrode achieves a peak power density of  $1.74 \text{ W cm}^{-2}$  at  $750^\circ\text{C}$  and an electrolysis current density of  $1.77 \text{ A cm}^{-2}$  at 1.3 V with excellent durability for 200 h. The combined decoration and direct assembly approach provides a unique and general pathway to develop a new class of nanostructured air electrodes for efficient and durable solid oxide cells.

## 1. Introduction

Effective and efficient utilization of renewable energy such as solar and wind power is vital to meet the ever increasing energy demand of the society and reduce the greenhouse emissions due to the excess use of fossil fuels. However, the intermittency and uneven distribution of renewable energy sources pose severe challenges to the main power facilities that need to continuously meet the power supply requirements [1]. Reversible solid oxide cells (SOCs) are an efficient energy conversion and storage device that can reasonably and efficiently utilize renewable energy [2–6]. SOCs can turn on the electrolysis mode to convert the excess electricity into fuels as the renewable electricity exceeds the demand, and switch to the fuel cell mode to convert the fuels into electricity when needed. This coordination makes the supply of renewable energy more flexible and stable.

However, one of the key obstacles in developing high performance SOCs is the sluggish kinetics of oxygen reduction reaction (ORR) and oxygen evolution reaction (OER) on the state-of-the-art air electrodes [7], and therefore, it is essential to develop alternative active air

electrode materials. In recent years, the family of cation-ordered double perovskite oxides  $\text{LnBaCo}_2\text{O}_{5+\delta}$  (LnBC, Ln=Pr, Gd, Sm, Nd, etc.) have attracted much interest [8–21], as they possess faster oxygen ion diffusion and surface exchange kinetics than commonly used  $\text{La}_{0.6}\text{Sr}_{0.4}\text{Co}_{0.2}\text{Fe}_{0.8}\text{O}_{3-\delta}$  (LSCF) air electrode for intermediate temperature SOCs [22]. However, LnBC suffers from performance instability due to the tendency of surface segregation of Ba cation and its interaction with volatile impurities [23–26]. The partial substitution of Ba with Ca to form  $\text{LnBa}_{1-x}\text{Ca}_x\text{Co}_2\text{O}_{5+\delta}$  such as  $\text{PrBa}_{0.8}\text{Ca}_{0.2}\text{Co}_2\text{O}_{5+\delta}$  (PBCC) dramatically enhances the operational stability and the tolerance against the attack by impurities such as  $\text{CO}_2$  [27–29].

The electrocatalytic activity of LnBC air electrode can be enhanced by tuning the electrode's composition and/or microstructure. It is reported that the incorporation of Sm or Gd doped ceria (SDC or GDC) enhances the electrocatalytic activity of LnBC [30–35], due to the fact that the electrochemical reaction primarily occurs at the LnBC/doped ceria (DCO)/air triple-phase boundary (TPB) [36]. The addition of DCO also remarkably reduces the thermal expansion of LnBC, mitigating the thermal mismatch between LnBC and electrolyte [30,32,33,37].

\* Corresponding authors.

E-mail addresses: [S.Jiang@curtin.edu.au](mailto:S.Jiang@curtin.edu.au) (S.P. Jiang), [kongfa.chen@fzu.edu.cn](mailto:kongfa.chen@fzu.edu.cn) (K. Chen).

<sup>1</sup> These authors contributed equally to this work.

Nanotechnology such as wet infiltration has been applied to engineer the electrode's microstructure [29,38–48]. Liu's group [29,44,46,49] observed that the infiltration of BaO and BaCoO<sub>3-δ</sub> nanoparticles dramatically enhances the ORR activity of PBCC electrodes. Zhang et al. [47] reported that PrBa<sub>0.5</sub>Sr<sub>0.5</sub>Co<sub>1.5</sub>Fe<sub>0.5</sub>O<sub>5+δ</sub> infiltrated yttria-stabilized zirconia (YSZ) backbone showed a low electrode polarization resistance of 0.03 Ω cm<sup>2</sup> with minimal degradation at 700 °C for 600 h. However, wet infiltration process requires many repeated infiltration/annealing cycles and may not be viable for commercial applications [50]. The loading of the infiltrated phase is also limited by the volume of open pores of the electrode coating and this puts a significant limitation on the optimum loading of the infiltrated phase, e.g., < 5–10 wt%. Moreover, the nanostructure formed by the infiltration technique is inherently not stable due to the unrestricted environment of the infiltrated nanoparticles [50,51]. In situ exsolution is an alternative technique to the formation of uniformly dispersed electrocatalytic nanoparticles on the electrode surface [52–60]. For example, substantial performance improvement has been reported for Ni exsolution on La<sub>0.52</sub>Sr<sub>0.28</sub>Ni<sub>0.06</sub>Ti<sub>0.94</sub>O<sub>3</sub> [61]. However, the in situ exsolution of electrocatalytically active nanoparticles relies on the exsolution of reducible metallic ions such as Ni, which limits the types and selection of active species. Most critically, the occurrence of in situ exsolution under reducing conditions makes it difficult to be applied on the air electrodes. Thus, the development of more effective and easily scalable fabrication techniques for efficient nanostructured air electrodes are urgently needed for efficient SOC.

Recently, we have demonstrated the feasibility of direct assembly approach on fabrication of high performance and stable nanostructured air electrodes without traditional high-temperature sintering step via the in situ formation of the electrode/electrolyte interface by the electrochemical polarization [62–68]. This novel approach not only bypasses the high temperature sintering step, but also enables the incorporation of active phases by decoration method without the limitation on loading and type of the phases. Here, a nanostructured GDC-PBCC composite air electrode is developed by the combination of decoration process rather than conventional mechanical mixing process and direct assembly approach without the conventional sintering process. We demonstrate that the in situ formation of intertwined core-shell type nanostructured multi-phase air electrode, including PBCC, GDC and BaCoO<sub>3-δ</sub> (BCO), with excellent electrode/electrolyte interface leads to remarkably enhanced electrocatalytic activity and operational stability of the air electrodes under reversible SOC operating conditions.

## 2. Experimental

### 2.1. Synthesis of powders and electrode inks

Pristine PrBa<sub>0.8</sub>Ca<sub>0.2</sub>Co<sub>2</sub>O<sub>5+δ</sub> (PBCC) powder was synthesized using a modified Pechini method. The starting chemicals were Pr(NO<sub>3</sub>)<sub>3</sub>·6H<sub>2</sub>O (Analytical Reagent, AR), Ba(NO<sub>3</sub>)<sub>2</sub> (AR), Ca(NO<sub>3</sub>)<sub>2</sub>·4H<sub>2</sub>O (AR), Co(NO<sub>3</sub>)<sub>3</sub>·6H<sub>2</sub>O (AR), citric acid (CA, AR), ethylenediamine tetraacetic acid (EDTA, AR), and ammonia solution (25–28 wt%). The molar ratio of metal ions: CA: EDTA was 1: 1.5: 1. The resultant powder was calcined at 1050 °C in air for 5 h to attain pure PBCC phase.

Gd<sub>0.2</sub>Ce<sub>0.8</sub>O<sub>1.9</sub> (GDC) decorated PBCC (GDC-PBCC) composite powders were synthesized using a sol-gel decoration approach. A GDC precursor solution was prepared by adding Gd(NO<sub>3</sub>)<sub>3</sub>·6H<sub>2</sub>O (AR), Ce(NO<sub>3</sub>)<sub>3</sub>·6H<sub>2</sub>O (AR), CA, EDTA and ammonia solution to deionized water with fixed molar ratio of metal ions: CA: EDTA at 1: 9: 6. The addition of such a high amount of CA and EDTA in the solution led to a much finer microstructure of as-synthesized composite powders and thereby a higher electrocatalytic performance (Fig. S1). The solution was stirred and heated on a hot plate to vaporize excessive water. An appropriate amount of PBCC powder was subsequently added to the viscous GDC precursor solution, followed by continuous stirring and heating. The resultant gel was dried in an oven at 180 °C for 12 h to obtain the black

foam ash. The ash was ground and calcined at 750 °C in air for 3 h to form the GDC-PBCC composite powder. A series of GDC-PBCC composites were synthesized with different GDC loadings of 10, 20, 30, 40, and 50 wt%, denoted as 10, 20, 30, 40, and 50GDC-PBCC, respectively. To prepare the GDC-PBCC air electrode ink, 60 wt% electrode powder was mixed with 40 wt% ink vehicle (4 wt% ethyl cellulose + 96 wt% terpineol) in a mortar.

### 2.2. Preparation and testing of hydrogen electrode-supported cells

NiO-YSZ hydrogen electrode-supported cells with the configuration of 0.8 mm thick NiO-YSZ support (NiO: YSZ: tapioca = 40: 40: 20, w/w/w)/11 μm thick NiO-YSZ functional layer (NiO: YSZ = 50: 50, w/w)/9 μm thick YSZ electrolyte film/~1 μm thick Gd<sub>0.1</sub>Ce<sub>0.9</sub>O<sub>1.95</sub> (GDC-b) buffer layer were prepared by slurry spin coating. The fabrication details can be found in our previous reports [69,70]. Porous and dense GDC-b buffer layers were prepared and the morphology of cross-sections of the cells is shown in Fig. S2. For the porous GDC-b buffer layer, the supported YSZ electrolyte films were sintered at 1450 °C in air for 5 h, and then the GDC-b ink was spin coated and sintered at 1150 °C for 2 h (Fig. S2a). In the case of the dense GDC-b buffer layer, the YSZ film and GDC-b layer were consecutively spin coated and the supported YSZ/GDC-b bilayers were co-sintered at 1400 °C in air for 2 h (Fig. S2b).

The air electrode ink was coated on the center of GDC-b buffer layer (0.22 cm<sup>2</sup>) and dried at 150 °C for 1 h without further sintering at high temperatures. The cells were sealed on a ceramic tube using a sealant (Ceramabond 552, Aremco) and heated to 750 °C in a tube furnace at a ramping rate of 5 °C min<sup>-1</sup>. The hydrogen electrodes were reduced at 750 °C for 1 h in 50 ml min<sup>-1</sup> wet hydrogen with 3 vol% steam. The discharge, charge curves and impedance spectra of the cells were measured at 600–750 °C using Gamry Interface 1000E. The cells' operating stability was performed in fuel cell mode and electrolysis mode under a constant current density of 0.5 A cm<sup>-2</sup> at 750 °C using Arbin BT-2000. The frequency of impedance measurements was 100 kHz–0.1 Hz and the AC amplitude was 10 mV. In fuel cell mode the hydrogen electrode was flowed with 50 ml min<sup>-1</sup> wet H<sub>2</sub>, while in electrolysis mode the hydrogen electrode with 50 ml min<sup>-1</sup> H<sub>2</sub> and 50 ml min<sup>-1</sup> CO<sub>2</sub> mixed gases. The feeding of H<sub>2</sub>-CO<sub>2</sub> mixture avoids the water supply in a humidifier and condensation of steam between the humidifier and the cells in the case of steam electrolysis. The air electrode was exposed to static surrounding air.

### 2.3. Phase and microstructure characterizations

The crystallographic phase of as-synthesized PBCC and GDC-PBCC powders were identified using X-ray diffraction (XRD, Rigaku Miniflex 600) with a Cu Kα X-ray source in a 2θ range of 20–80 degrees. The morphology and elemental distribution of 20GDC-PBCC powder were analyzed using field-emission transmission electron microscopy (TEM, FEI Tecnai G2F20 and Talos F200i) with high-resolution TEM (HRTEM) and high angle annular dark field (HAADF) scanning transmission electron microscopy (HAADF-STEM). The morphology of the as-prepared air electrodes calcined at 750 °C for 0.5 h was investigated using a scanning electron microscopy (SEM, Carl Zeiss SUPRA 55). Brunauer–Emmett–Teller (BET) measurements (Micromeritics ASAP 2460) were conducted to examine the specific surface areas of as-prepared powders. The samples were first degassed in vacuum at 320 °C for 12 h, and adsorbed with nitrogen at an adsorption temperature of 77.3 K.

X-ray absorption fine structure (XAFS) of PBCC and 20GDC-PBCC powders was collected at the beamline BL07A of Taiwan Light Source, National Synchrotron Radiation Research Center (NSRRC). The experiments were carried out in a transmission mode for Co K-edge and in a fluorescence mode for Ce L<sub>3</sub>-edge with a Lytle detector using a Si (111) double crystal monochromator. All the spectra were performed in ambient conditions. A Co foil was measured simultaneously to serve as

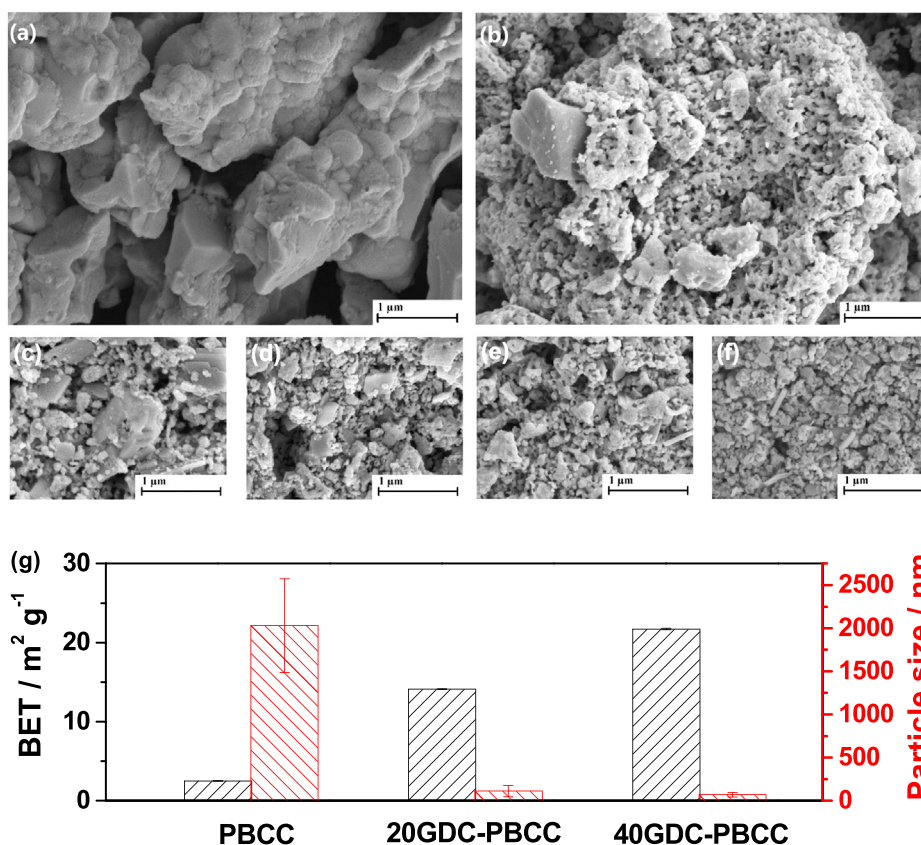


**Fig. 1.** SEM images of surface of as prepared air electrodes: (a) PBCC, (b) 10GDC-PBCC, (c) 20GDC-PBCC, (d) 30GDC-PBCC, (e) 40GDC-PBCC, and (f) 50GDC-PBCC. (g) BET and average particle size of as prepared PBCC and GDC-PBCC powders.

an energy reference for Co.

### 3. Results and discussion

#### 3.1. Microstructure characterization and phase identification

Fig. 1 shows the microstructure of as prepared PBCC and GDC-PBCC composite electrodes. The pristine PBCC electrode has severely agglomerated particles in an average size of  $2.03 \mu\text{m}$  (Fig. 1a), consistent with the morphology of as-synthesized PBCC powder (Fig. S3). However, after the decoration of 10 wt% GDC, a great number of nanoparticles appear with the absence of the original large PBCC particles (Fig. 1b). With increasing the GDC loading to 20–50 wt%, the electrode's microstructure becomes much finer (Fig. 1c–f), as is evident by the smaller particle size and greater specific surface area (Fig. 1g). The particle size and specific surface area of 40GDC-PBCC are 70 nm and  $21.71 \text{ m}^2 \text{g}^{-1}$ , respectively, dramatically different to those of  $2.03 \mu\text{m}$  and  $2.54 \text{ m}^2 \text{g}^{-1}$  of pristine PBCC.

The most important observation is the unique microstructure formed by the combined decoration and direct assembly method. Fig. 2 shows the microstructural observations and elemental maps of 20GDC-PBCC powder. The morphology of 20GDC-PBCC is characterized by the existence of highly porous nanoclusters, which are likely related to small PBCC particles (in a size of  $100 \pm 20 \text{ nm}$ ), decorated by very fine nanoparticles (Fig. 2a). HRTEM analysis on the edge of 20GDC-PBCC powder indicates the presence of PBCC phase with the observed  $d$ -space of PBCC (100) plane of 0.388 nm (Fig. 2b), slightly smaller than 0.39 nm of pristine PBCC [29]. In addition to the PBCC phase, GDC and  $\text{BaCoO}_{3.8}$  (BCO) were also detected (Fig. 2b), demonstrating the fine nanoparticles are ascribed to the homogeneous mixture of the multi-phases and the formation of an intertwined core-shell type nanostructure of GDC-PBCC composite.

Fig. 3 shows the XRD patterns of PBCC and GDC-PBCC powders. The PBCC powder displays a group of diffraction peaks identical to the  $P4/\text{mmm}$  space group of layered perovskite structure [29]. However, in the GDC-PBCC powders calcined at  $750^\circ\text{C}$ , new phase of BCO appears in addition to the GDC and PBCC phases (Fig. 3a). The existence of multi-phases is consistent with the HRTEM observations (see Fig. 2b). The relative peak intensities of GDC (111) and BCO (110) to PBCC (102) increase with increasing the GDC loading (Fig. 3b), indicating the gradual increase of GDC and BCO loadings in GDC-PBCC. In GDC-PBCC, the PBCC (102) diffraction peak shifts to a higher angle, indicating the contraction of PBCC lattice by the GDC decoration, in agreement with the HRTEM observations (see Fig. 2b). It is worthwhile noting that at a lower calcination temperature of  $650^\circ\text{C}$ , there is a dramatic increase of relative diffraction intensity of GDC (111) to PBCC (102) (Fig. S4). This implies that a proportion of PBCC particles is decomposed during the decoration process, though a majority of the PBCC phase is reformed after the calcination at higher temperature of  $750^\circ\text{C}$ .

To explore the reason of decomposition of PBCC phase during GDC decoration, a certain amount of PBCC powder was added to an aqueous solution containing  $\text{Gd}(\text{NO}_3)_3$ ,  $\text{Ce}(\text{NO}_3)_3$ , citric acid, EDTA and ammonia, identical to that used for the preparation of 20GDC-PBCC powder. The mixed PBCC-soaking solution was stirred on a hot plate for different periods and the undissolved PBCC powder was collected by filtering the suspension solution. It is observed that the particle size of undissolved PBCC powder decreases with increasing the soaking time (Fig. S5a–e). The partial dissolution of PBCC is primarily ascribed to the acidic nature of the soaking solution. The initial pH value of the soaking solution is 3.15 and increases with increasing the soaking time (Fig. S5f). It is worthwhile noting that the crystalline phase and composition of undissolved PBCC powder are intact (Fig. S6 and Table S1), implying the dissolution of PBCC particles is proceeded in a layer-by-layer fashion.

Due to the nature of in situ exsolution, GDC phase cannot be formed



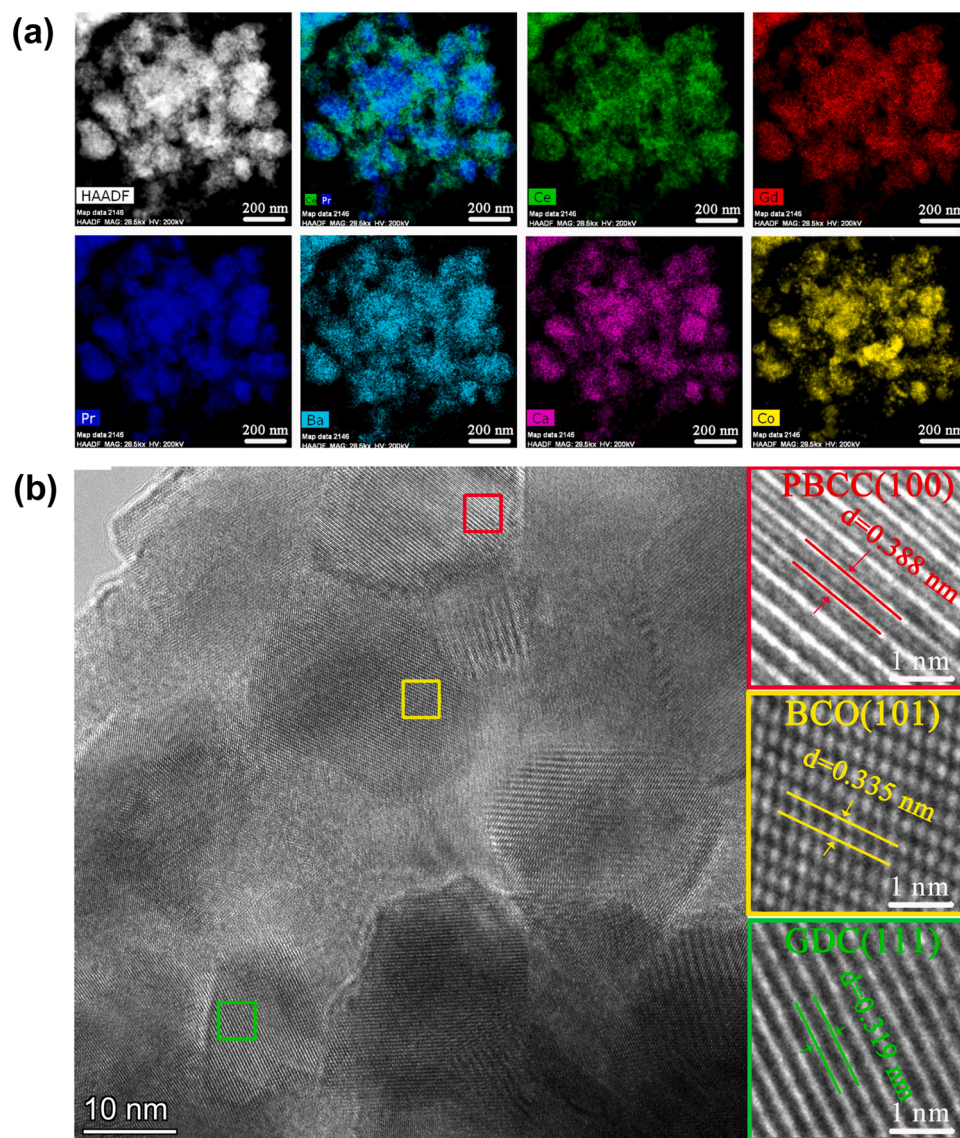


Fig. 2. (a) HAADF image and EDS elemental maps and (b) HRTEM image of 20GDC-PBCC powder.

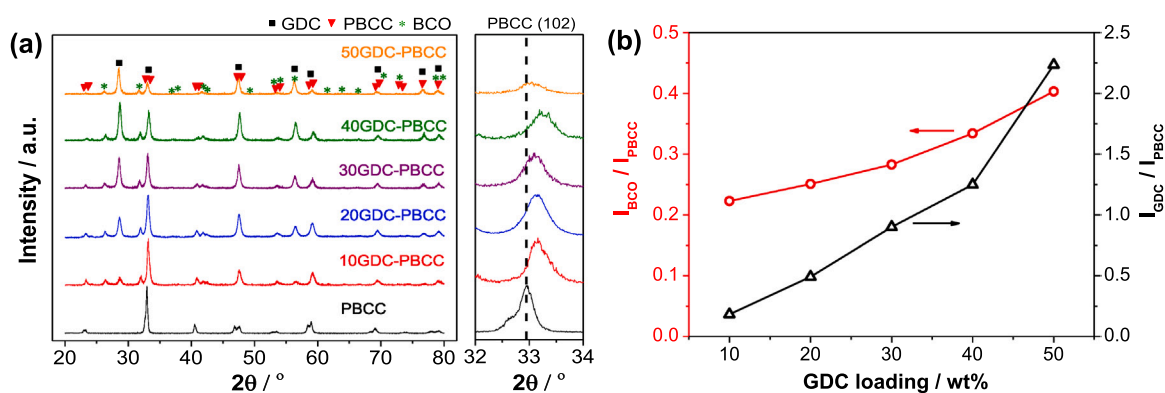
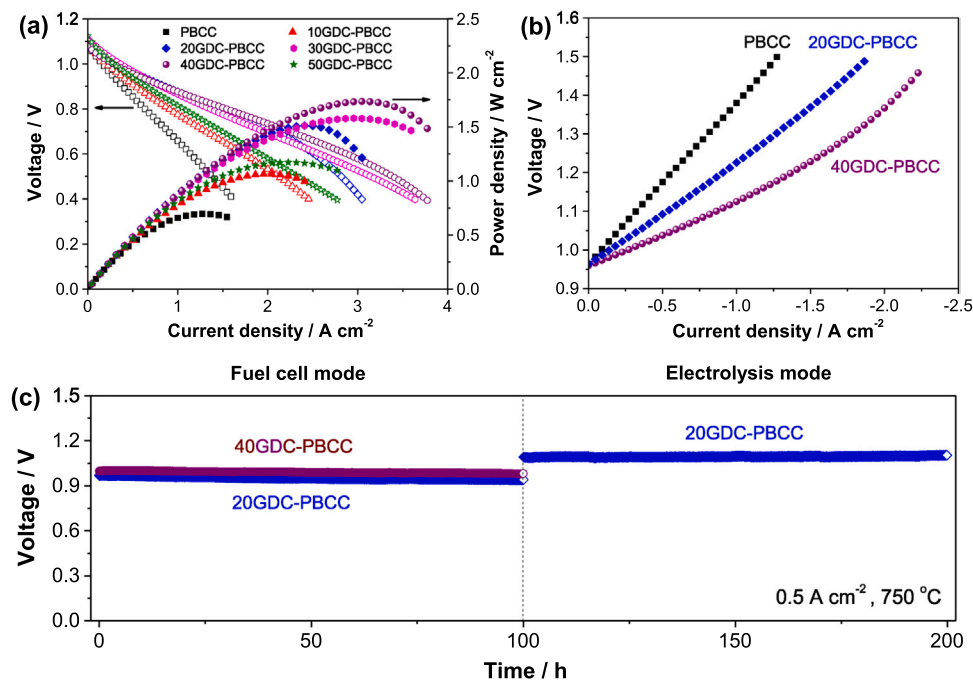


Fig. 3. (a) XRD patterns of as prepared PBCC powder and GDC-PBCC powders. (b) Relative peak intensity of BCO (110) and GDC (111) to PBCC (102) as a function of GDC loading.

on the PBCC surface by in situ exsolution under cathodic oxidation conditions. GDC nanoparticles can be introduced to the PBCC electrode by infiltration, but the loading of infiltrates is generally limited. The fabrication of electrode using the mechanical mixing leads to a poor

interface between PBCC and GDC dual phases due to the intrinsic nature of the mechanical mixing process [71]. As shown in this study, it is clear that during the GDC decoration process a proportion of PBCC particles was dissolved in a layer-by-layer fashion and mixed uniformly with the



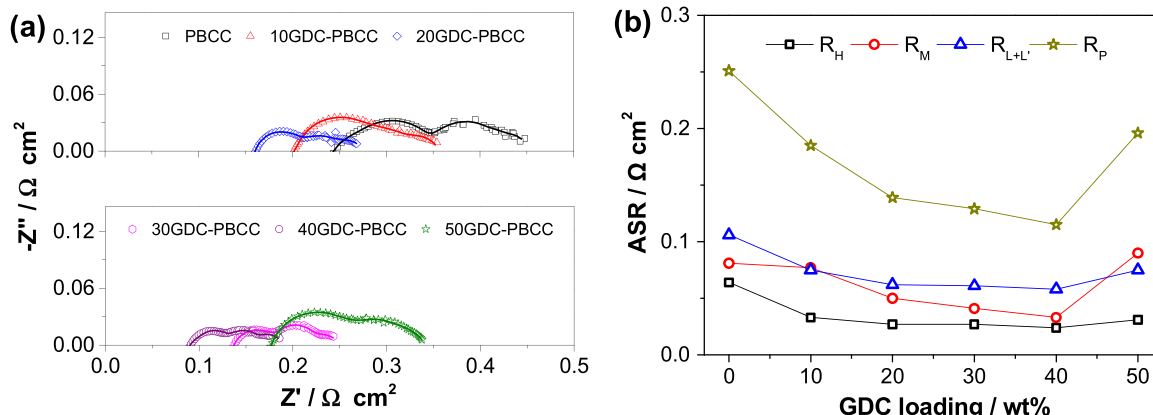
**Fig. 4.** (a) Discharge curves and (b) charge curves of PBCC and GDC-PBCC cells measured at 750 °C. (c) Stability curves of 20 and 40GDC-PBCC cells in fuel cell and electrolysis modes.

decorated GDC nitrates, leading to the in situ formation of ultrafine and unique nanostructured GDC-PBCC composite and intimate interface between the PBCC and decorated GDC phases (see Fig. 1). The interaction between PBCC and GDC phases is also revealed by the XAFS spectra of Co K-edge and Ce L<sub>3</sub>-edge of PBCC and 20GDC-PBCC powders (Fig. S7). The results demonstrate the significant advantages of the combined decoration and direct assembly techniques in the fabrication of unique intertwined core-shell type nanostructured multi-phase GDC-PBCC composite electrodes with intimate electrode/electrolyte interface, which would not be possible with the wet infiltration and in situ exsolution techniques.

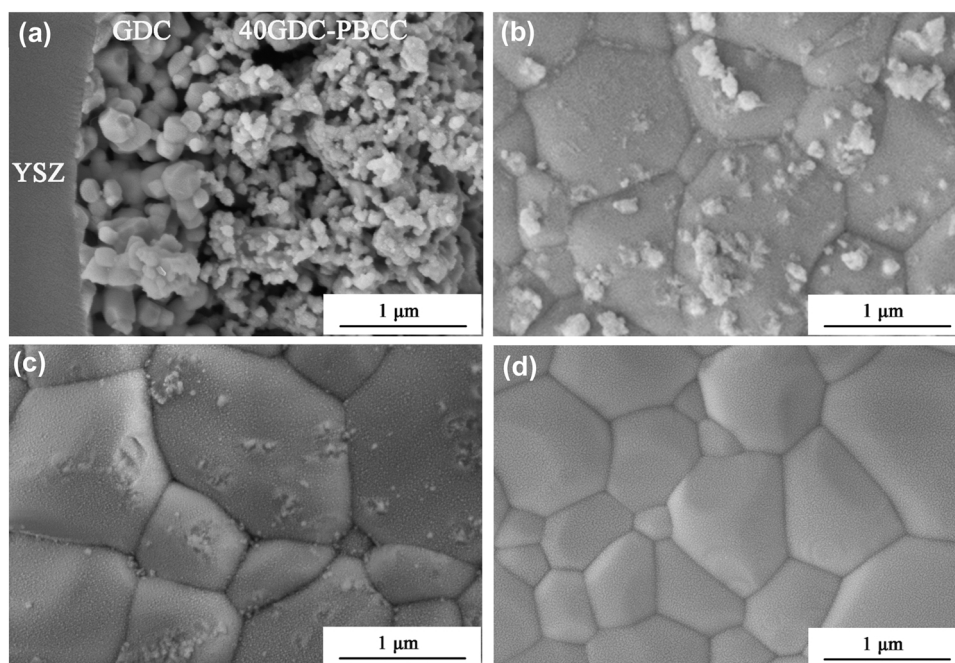
### 3.2. Electrochemical performance and stability

Fig. 4 shows the discharge and charge performance and stability curves of directly assembled pristine PBCC and GDC-PBCC cells with 10–50 wt% decorated GDC measured at 750 °C. The pristine PBCC cell achieves a peak power density (PPD) of 0.69 W cm<sup>-2</sup>, lower than those of the sintered PBCC cells reported by Liu's group [44,46,72]. Liu's group sintered the PBCC air electrodes on YSZ/Sm<sub>0.2</sub>Ce<sub>0.8</sub>O<sub>1.9</sub> (SDC),

Sc<sub>0.1</sub>Zr<sub>0.9</sub>O<sub>2</sub> (ScSZ)/SDC, and SDC electrolyte films at 900–1000 °C, and the single cells reached the PPDs of 0.85, 0.94, and 1.15 W cm<sup>-2</sup> at 750 °C, respectively [44,46,72]. The lower PPD of the pristine PBCC cell in this work could be ascribed to the significantly coarsened microstructure of PBCC electrode as the PBCC powder was calcined at 1050 °C (Figs. 1a and S3), much higher than the calcination temperatures of the PBCC powder (800 °C) and the sintering temperatures of the electrodes (900–1000 °C) reported by Liu's group [44,46,72]. On the other hand, the 10, 20, 30, 40 and 50GDC-PBCC cells reach PPDs of 1.07, 1.51, 1.58, 1.74, and 1.17 W cm<sup>-2</sup>, respectively, dramatically higher than 0.69 W cm<sup>-2</sup> of the pristine PBCC cell (Fig. 4a). Furthermore, the electrolysis performance of GDC-PBCC cells also outperforms that of the PBCC cell (Figs. 4b and S8). The 20 and 40GDC-PBCC cells exhibit an electrolysis current density of 1.27 and 1.77 A cm<sup>-2</sup> at 1.3 V, respectively, much higher than 0.82 A cm<sup>-2</sup> of the PBCC cell. More importantly, the 20 and 40GDC-PBCC cells show excellent stability without degradation during the galvanostatic tests at 750 °C and 0.5 A cm<sup>-2</sup> in fuel cell mode for 100 h, and the 20GDC-PBCC cell is also stable during the operation in electrolysis mode for another 100 h (Fig. 4c). The high operating stability of the cells with nanostructured GDC-PBCC air



**Fig. 5.** (a) Nyquist plots of PBCC and GDC-PBCC cells measured at 750 °C. (b)  $R_H$ ,  $R_M$ ,  $R_{L+L'}$ , and  $R_P$  curves as a function of GDC loading.



**Fig. 6.** SEM images of 40GDC-PBCC cells after polarization in fuel cell mode at 750 °C and 0.5 A cm<sup>-2</sup> for 100 h. (a) Cross-section of 40GDC-PBCC cell with a porous GDC-b buffer layer. Surface of dense GDC-b buffer layer after removing the air electrode (b) by adhesive tape and (c) by acid treatment. (d) Surface of bare dense GDC-b buffer layer without coating the air electrode.

electrodes is a clear indication that the intertwined core-shell type nanostructures inhibit the agglomeration of the PBCC and GDC nanoparticles in the composites, as shown in Fig. 2b. This demonstrates the great potential of the GDC-PBCC composite with a unique microstructure as an efficient and durable air electrode for reversible SOCs.

As the difference of PBCC and GDC-PBCC cells is only the air electrodes, the much higher fuel cell and electrolysis performances of GDC-PBCC cells than those of pristine PBCC cell demonstrates the significantly enhanced electrocatalytic activity of PBCC by the GDC decoration. Fig. 5a shows the Nyquist plots of the impedance spectra as a function of GDC loading. It is observed that the GDC decoration leads to a decrease of both cell ohmic and polarization resistances,  $R_{\Omega}$  and  $R_p$ .  $R_{\Omega}$  of the PBCC cell is 0.204  $\Omega$  cm<sup>2</sup>, and decreases to 0.172, 0.133, 0.111, 0.075 and 0.145  $\Omega$  cm<sup>2</sup> for 10, 20, 30, 40 and 50GDC-PBCC cells, respectively.  $R_{\Omega}$  is related to the overall ohmic resistances from the electrodes, electrolyte, and contacts of electrode/electrolyte interfaces and electrode/current collector interfaces. As the air electrode/current collector interface is identical for the cells, the difference in  $R_{\Omega}$  is primarily attributed to the variation at the air electrode/electrolyte interface. The decrease in  $R_{\Omega}$  with increasing the GDC loading is probably ascribed to the unique interfacial contact, as a result of the combined decoration and direct assembly fabrication processes (see Fig. 1a). On the other hand,  $R_{\Omega}$  of the GDC-PBCC cells starts to increase as the GDC loading exceeds 40 wt%, due to the fact that the presence of excessive GDC hinders the connectivity of electronic network in the composite electrode. The GDC decoration also leads to a decrease of  $R_p$ .  $R_p$  of the PBCC cell is 0.251  $\Omega$  cm<sup>2</sup>, and decreases to 0.185, 0.139, 0.136, 0.115 and 0.196  $\Omega$  cm<sup>2</sup> for the 10, 20, 30, 40 and 50GDC-PBCC cells, respectively.

According to the distribution relaxation times (DRT) analysis (Fig. S9), the impedance spectra display four distinct peaks at high frequency (HF), medium frequency (MF), low frequency (LF) and extra low frequency (L/F). It appears that except the HF arcs, the MF, LF and L/F arcs are subjected to the variation of atmospheres in both hydrogen and air electrodes (Fig. S9). The HF arc is likely associated with oxygen ion transfer across the air electrode/electrolyte interface, the MF arc is partly related to the adsorption and dissociation of oxygen molecules,

and the LF and L/F arcs are attributed to the gas diffusion and conversion processes within the pores of electrodes [29,44,46,72]. The impedance spectra are fitted using an equivalent circuit with four  $R_iQ_i$  elements ( $i = H, M, L$  and  $L'$ ) together with a  $R_{\Omega}$  and an inductor  $L$ , where  $Q$  represents a constant phase element. The fitting results are summarized in Table S2 and Fig. 5b.

Generally,  $R_H$ ,  $R_M$  and  $R_{L+L'}$  decrease as the GDC loading increases from 0 to 40 wt%, but they increase with the further increase of GDC loading up to 50 wt% (Fig. 5b). However, the magnitude of changes is different for the electrode processes.  $R_H$  and  $R_{L+L'}$  decrease distinctly at GDC loading of 10 wt%, and remain more or less stable with the further increase of GDC loading. The ultrafine microstructure of GDC-PBCC electrode enhances the interfacial contact, as is indicated by the significant lower  $R_{\Omega}$  than that of PBCC, and therefore, the oxygen ion transfer process at the air electrode/electrolyte interface related to  $R_H$  is remarkably facilitated. Furthermore, the highly porous structure of GDC-PBCC electrode is beneficial to rapid gas diffusion, in contrast to the limited gas diffusion pathway in the severely agglomerated pristine PBCC electrode, and therefore,  $R_{L+L'}$  of GDC-PBCC cells is reduced. On the other hand,  $R_M$  decreases continuously and distinctly with the increase of GDC loading up to 40 wt%, followed by an abrupt increase as the GDC loading reaches 50 wt%. The PBCC/GDC/air TPBs are the major sites for the ORR and OER [36], and the nanoscale GDC and PBCC phases dramatically increase the TPB length [73,74]. Therefore, the oxygen surface exchange ability of ultrafine GDC-PBCC electrode is greatly enhanced [36]. This is also supported by the fact the increase of the calcination temperature of GDC-PBCC powder significantly coarsens the electrode microstructure, leading to an increase of  $R_M$  and a decrease of PPD (Fig. S10). Furthermore, as BCO possess stronger oxygen absorption and desorption ability than PBCC [29,44,46,49], the presence of BCO nanoparticles also boosts the surface exchange process of PBCC. Therefore, the formation of ultrafine microstructure and the presence of catalytically active BCO nanoparticles lead to the decrease of  $R_M$  of GDC-PBCC cells.



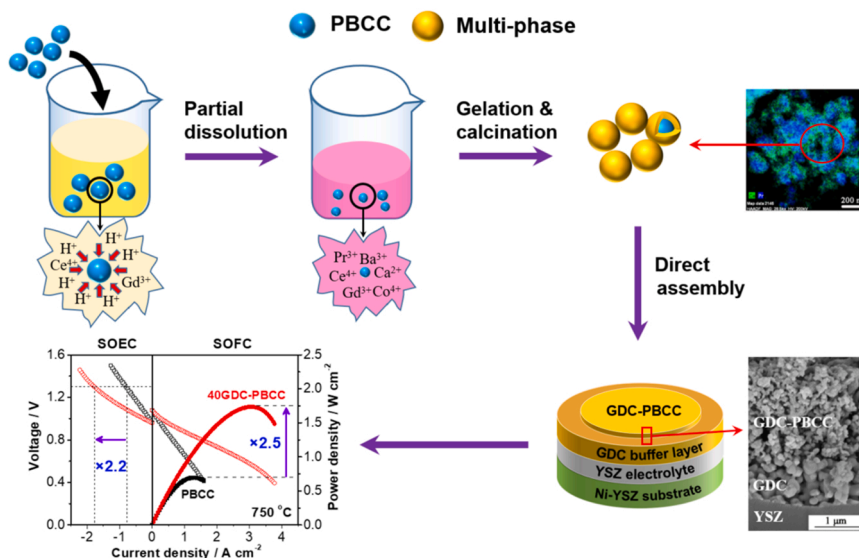


Fig. 7. A scheme of the combined decoration and direct assembly approach for the fabrication of multi-phase GDC-PBCC composite electrodes.

### 3.3. Electrode/electrolyte interface formation

Fig. 6a shows the cross section of air electrode/electrolyte interface of the 40GDC-PBCC cell after polarization at 750 °C in fuel cell mode for 100 h. Intimate interfacial contact is formed between post-mortem 40GDC-PBCC electrode and porous GDC-b buffer layer, and the ultra-fine electrode microstructure is retained. The particle size of polarized 40GDC-PBCC electrode is  $72 \pm 22$  nm, close to  $70 \pm 26$  nm that of as prepared electrode. To clearly observe the interfacial contact, a 40GDC-PBCC electrode was directly assembled on a cell with a dense GDC-b buffer layer and the cell was operated under identical conditions for 100 h. After the post-mortem 40GDC-PBCC electrode is separated, there are some remaining particles on the surface of GDC layer (Fig. 6b). The removal of these surface particles by soaking them in HCl acid leads to the exposure of distinct contact marks on the electrolyte surface (Fig. 6c), very different to the morphology of bare GDC layer (Fig. 6d). The size of contact marks is  $120 \pm 35$  nm, close to  $110 \pm 37$  nm of the surface particles. This indicates the strong interaction between the surface particles and GDC-b buffer layer, an indication of forming an intimate electrode/electrolyte interface by the polarization [75,76].

Fig. 7 shows a scheme of the combined decoration and direct assembly approach used for the fabrication of nanostructured multi-phase GDC-PBCC composite electrodes. The decoration process is part of the powder mixture process, thus avoiding the limitation of loading in the wet infiltration method and limited types of active phases in the case of in situ exsolution method. The partial surface decomposition of PBCC phase and uniform mixing with decorated GDC nitrate solution lead to the in situ formation of an intertwined core-shell type nanostructure with PBCC, GDC, and BCO multi-phases. Due to the fact that the electrode/electrolyte interface is induced by the polarization under fuel cell operating conditions, the unique nanostructure of the green powder and coating structures can be largely retained, leading to the remarkably enhanced electrocatalytic activity and operational stability of the nanostructured multi-phase GDC-PBCC air electrodes (see Figs. 4 and 6).

## 4. Conclusions

A new class of intertwined nanostructured multi-phase air electrode, consisting of PBCC, GDC and BCO, is successfully fabricated by a facile combined decoration and direct assembly approach, without the conventional high temperature sintering process and limitation in the loading of decorated GDC phase. Due to the acidic nature of the GDC precursor solution, PBCC is partially dissolved during the decoration

process, leading to homogeneous mixture and formation of PBCC, GDC and BCO nanoparticles with a unique intertwined ultrafine electrode microstructure. The best performance is obtained on the cell with 40GDC-PBCC air electrode, achieving a PPD of  $1.74 \text{ W cm}^{-2}$  at 750 °C and an electrolysis current density of  $1.77 \text{ A cm}^{-2}$  at 1.3 V with excellent stability in fuel cell and electrolysis modes for 200 h. The present work provides a facile and effective means to design highly active and stable air electrodes with unique intertwined core-shell type nanostructures, which can be applied in general on the development of nanostructured air electrodes for efficient and durable SOCs.

### CRediT authorship contribution statement

**Zhiyi Chen:** Investigation, Data curation, Writing – original draft. **Lizhen Jiang:** Investigation, Data curation, Formal analysis. **Shuai He:** Investigation, Data curation. **Chengzhi Guan:** Data curation, Resources. **Yuanfeng Zou:** Investigation, Data curation. **Zhongwei Yue:** Investigation, Data curation. **Na Ai:** Methodology, Resources. **San Ping Jiang:** Supervision, Writing – review & editing. **Yanqun Shao:** Formal analysis. **Kongfa Chen:** Supervision, Conceptualization, Writing – review & editing, Funding acquisition.

### Declaration of Competing Interest

The authors declare that they have no known competing financial interests or personal relationships that could have appeared to influence the work reported in this paper.

### Acknowledgements

The project was supported by the National Natural Science Foundation of China (21875038 and 22005055), and the Australian Research Council (DP180100731 and DP180100568). The authors acknowledge Shih-Chang Weng and Yun-Liang Soo for excellent experimental support at BL-07A of the NSRRC.

### Appendix A. Supporting information

Supplementary data associated with this article can be found in the online version at doi:10.1016/j.apcatb.2021.121056.

## References

- [1] A. Hauch, R. Küngas, P. Blennow, A.B. Hansen, J.B. Hansen, B.V. Mathiesen, M. B. Mogensen, Recent advances in solid oxide cell technology for electrolysis, *Science* 370 (2020), eaba6118.
- [2] M.A. Laguna-Bercero, Recent advances in high temperature electrolysis using solid oxide fuel cells: a review, *J. Power Sources* 203 (2012) 4–16.
- [3] S.D. Ebbesen, S.H. Jensen, A. Hauch, M.B. Mogensen, High temperature electrolysis in alkaline cells, solid proton conducting cells, and solid oxide cells, *Chem. Rev.* 114 (2014) 10697–10734.
- [4] Y. Zheng, J. Wang, B. Yu, W. Zhang, J. Chen, J. Qiao, J. Zhang, A review of high temperature co-electrolysis of H<sub>2</sub>O and CO<sub>2</sub> to produce sustainable fuels using solid oxide electrolysis cells (SOECs): advanced materials and technology, *Chem. Soc. Rev.* 46 (2017) 1427–1463.
- [5] Y. Wang, D.Y.C. Leung, J. Xuan, H. Wang, A review on unitized regenerative fuel cell technologies, part B: unitized regenerative alkaline fuel cell, solid oxide fuel cell, and microfluidic fuel cell, *Renew. Sustain. Energy Rev.* 75 (2017) 775–795.
- [6] T. Mori, R. Wepf, S.P. Jiang, Future prospects for the design of ‘state-of-the-art’ solid oxide fuel cells, *J. Phys. Energy* 2 (2020), 031001.
- [7] Y. Chen, W. Zhou, D. Ding, M. Liu, F. Ciucci, M. Tade, Z. Shao, Advances in cathode materials for solid oxide fuel cells: complex oxides without alkaline earth metal elements, *Adv. Energy Mater.* 5 (2015), 1500537.
- [8] A. Tarancon, M. Burriel, J. Santiso, S.J. Skinner, J.A. Kilner, Advances in layered oxide cathodes for intermediate temperature solid oxide fuel cells, *J. Mater. Chem.* 20 (2010) 3799–3813.
- [9] C. Zhu, X. Liu, C. Yi, D. Yan, W. Su, Electrochemical performance of PrBaCo<sub>2</sub>O<sub>5+δ</sub> layered perovskite as an intermediate-temperature solid oxide fuel cell cathode, *J. Power Sources* 185 (2008) 193–196.
- [10] K. Zhang, L. Ge, R. Ran, Z. Shao, S. Liu, Synthesis, characterization and evaluation of cation-ordered LnBaCo<sub>2</sub>O<sub>5+δ</sub> as materials of oxygen permeation membranes and cathodes of SOFCs, *Acta Mater.* 56 (2008) 4876–4889.
- [11] L. Zhao, B. He, B. Lin, H. Ding, S. Wang, Y. Ling, R. Peng, G. Meng, X. Liu, High performance of proton-conducting solid oxide fuel cell with a layered PrBaCo<sub>2</sub>O<sub>5+δ</sub> cathode, *J. Power Sources* 194 (2009) 835–837.
- [12] D. Chen, R. Ran, K. Zhang, J. Wang, Z. Shao, Intermediate-temperature electrochemical performance of a polycrystalline PrBaCo<sub>2</sub>O<sub>5+δ</sub> cathode on samarium-doped ceria electrolyte, *J. Power Sources* 188 (2009) 96–105.
- [13] H. Ding, X. Xue, PrBa<sub>0.5</sub>Sr<sub>0.5</sub>Co<sub>2</sub>O<sub>5+δ</sub> layered perovskite cathode for intermediate temperature solid oxide fuel cells, *Electrochim. Acta* 55 (2010) 3812–3816.
- [14] L. Jiang, F. Li, T. Wei, R. Zeng, Y. Huang, Evaluation of Pr<sub>1-x</sub>Ba<sub>x</sub>Co<sub>2</sub>O<sub>5+δ</sub> (x=0–0.30) as cathode materials for solid-oxide fuel cells, *Electrochim. Acta* 133 (2014) 364–372.
- [15] M. Li, K. Chen, B. Hua, J.-I. Luo, W.D.A. Rickard, J. Li, J.T.S. Irvine, S.P. Jiang, Smart utilization of cobaltite-based double perovskite cathodes on barrier-layer-free zirconia electrolyte of solid oxide fuel cells, *J. Mater. Chem. A* 4 (2016) 19019–19025.
- [16] J.T.S. Irvine, J. Bae, J.-Y. Park, W.S. Choi, J.H. Kim, Electrochemical properties and durability of in-situ composite cathodes with SmBa<sub>0.5</sub>Sr<sub>0.5</sub>Co<sub>2</sub>O<sub>5+δ</sub> for metal supported solid oxide fuel cells, *Int. J. Hydrog. Energy* 42 (2017) 1212–1220.
- [17] J.Y. Chen, J. Li, L.C. Jia, I. Moussa, B. Chi, J. Pu, J. Li, A novel layered perovskite Nd(Ba<sub>0.4</sub>Sr<sub>0.4</sub>Ca<sub>0.2</sub>)Co<sub>1.6</sub>Fe<sub>0.4</sub>O<sub>5+δ</sub> as cathode for proton-conducting solid oxide fuel cells, *J. Power Sources* 428 (2019) 13–19.
- [18] W. Tang, H. Ding, W. Bian, W. Wu, W. Li, X. Liu, J.Y. Gomez, C.Y.R. Vera, M. Zhou, D. Ding, Understanding of A-site deficiency in layered perovskites: promotion of dual reaction kinetics for water oxidation and oxygen reduction in protonic ceramic electrochemical cells, *J. Mater. Chem. A* 8 (2020) 14600–14608.
- [19] Y. Tian, Y. Liu, W. Wang, L. Jia, J. Pu, B. Chi, J. Li, High performance and stability of double perovskite-type oxide NdBa<sub>0.5</sub>Ca<sub>0.5</sub>Co<sub>1.5</sub>Fe<sub>0.5</sub>O<sub>5+δ</sub> as an oxygen electrode for reversible solid oxide electrochemical cell, *J. Energy Chem.* 43 (2020) 108–115.
- [20] W. Zhang, Y. Zhou, E. Liu, Y. Ding, Z. Luo, T. Li, N. Kane, B. Zhao, Y. Niu, Y. Liu, M. Li, A Highly Efficient and Durable Air Electrode for Intermediate-temperature Reversible Solid Oxide Cells, *Appl. Catal. B Environ.* 299 (2021), 120631.
- [21] S. Wang, J. Zan, W. Qiu, D. Zheng, F. Li, W. Chen, Q. Pei, L. Jiang, Evaluation of perovskite oxides LnBaCo<sub>2</sub>O<sub>5+δ</sub> (Ln = La, Pr, Nd and Sm) as cathode materials for IT-SOFC, *J. Electroanal. Chem.* 886 (2021), 115144.
- [22] G. Kim, S. Wang, A.J. Jacobson, L. Reimus, P. Brodersen, C.A. Mims, Rapid oxygen ion diffusion and surface exchange kinetics in PrBaCo<sub>2</sub>O<sub>5+x</sub> with a perovskite related structure and ordered A cations, *J. Mater. Chem.* 17 (2007) 2500–2505.
- [23] J. Druce, H. Tellez, M. Burriel, M.D. Sharp, L.J. Fawcett, S.N. Cook, D.S. McPhail, T. Ishihara, H.H. Brongersma, J.A. Kilner, Surface termination and subsurface restructuring of perovskite-based solid oxide electrode materials, *Energy Environ. Sci.* 7 (2014) 3593–3599.
- [24] H. Tellez, J. Druce, J.A. Kilner, T. Ishihara, Relating surface chemistry and oxygen surface exchange in LnBaCo<sub>2</sub>O<sub>5+δ</sub> air electrodes, *Faraday Discuss.* 182 (2015) 145–157.
- [25] B. Wei, K. Chen, C.C. Wang, Z. Lü, S.P. Jiang, Performance degradation of SmBaCo<sub>2</sub>O<sub>5+δ</sub> cathode induced by chromium deposition for solid oxide fuel cells, *Electrochim. Acta* 174 (2015) 327–331.
- [26] L. Zhu, B. Wei, Z. Wang, K. Chen, H. Zhang, Y. Zhang, X. Huang, Z. Lü, Electrochemically driven deactivation and recovery in PrBaCo<sub>2</sub>O<sub>5+δ</sub> oxygen electrodes for reversible solid oxide fuel cells, *ChemSusChem* 9 (2016) 2443–2450.
- [27] S. Yoo, A. Jun, Y.-W. Ju, D. Odkhuu, J. Hyodo, H.Y. Jeong, N. Park, J. Shin, T. Ishihara, G. Kim, Development of double-perovskite compounds as cathode materials for low-temperature solid oxide fuel cells, *Angew. Chem. Int. Ed.* 53 (2014) 13064–13067.
- [28] S. Choi, S. Park, J. Shin, G. Kim, The effect of calcium doping on the improvement of performance and durability in a layered perovskite cathode for intermediate-temperature solid oxide fuel cells, *J. Mater. Chem. A* 3 (2015) 6088–6095.
- [29] Y. Chen, Y. Choi, S. Yoo, Y. Ding, R. Yan, K. Pei, C. Qu, L. Zhang, I. Chang, B. Zhao, Y. Zhang, H. Chen, Y. Chen, C. Yang, B. deGlee, R. Murphy, J. Liu, M. Liu, A highly efficient multi-phase catalyst dramatically enhances the rate of oxygen reduction, *Joule* 2 (2018) 938–949.
- [30] D. Chen, R. Ran, Z. Shao, Assessment of PrBaCo<sub>2</sub>O<sub>5+δ</sub>+Sm<sub>0.2</sub>Ce<sub>0.8</sub>O<sub>1.9</sub> composites prepared by physical mixing as electrodes of solid oxide fuel cells, *J. Power Sources* 195 (2010) 7187–7195.
- [31] S. Lü, G. Long, Y. Ji, X. Meng, C. Sun, Characterization of SmBaCoFeO<sub>5+δ</sub>-Ce<sub>0.9</sub>Gd<sub>0.1</sub>O<sub>1.95</sub> composite cathodes for intermediate-temperature solid oxide fuel cells, *Int. J. Hydrog. Energy* 35 (2010) 7930–7935.
- [32] N. Li, B. Wei, Z. Lü, X. Huang, W. Su, GdBaCo<sub>2</sub>O<sub>5+δ</sub>-Sm<sub>0.2</sub>Ce<sub>0.8</sub>O<sub>1.9</sub> composite cathodes for intermediate temperature SOFCs, *J. Alloy. Compd.* 509 (2011) 3651–3655.
- [33] J. Kim, W.Y. Seo, J. Shin, M.L. Liu, G. Kim, Composite cathodes composed of NdBa<sub>0.5</sub>Sr<sub>0.5</sub>Co<sub>2</sub>O<sub>5+δ</sub> and Ce<sub>0.9</sub>Gd<sub>0.1</sub>O<sub>1.95</sub> for intermediate-temperature solid oxide fuel cells, *J. Mater. Chem. A* 1 (2013) 515–519.
- [34] B. Wei, Z. Lü, W. Jiang, X. Zhu, W. Su, Functionally graded cathodes based on double perovskite type GdBaCo<sub>2</sub>O<sub>5+δ</sub> oxide, *Electrochim. Acta* 134 (2014) 136–142.
- [35] A. Jun, J. Kim, J. Shin, G. Kim, Achieving high efficiency and eliminating degradation in solid oxide electrochemical cells using high oxygen-capacity perovskite, *Angew. Chem. Int. Ed.* 55 (2016) 12512–12515.
- [36] Y. Wan, B. Hu, C. Xia, Oxygen reduction at the three-phase boundary of PrBaCo<sub>2</sub>O<sub>5+δ</sub>-Sm<sub>0.2</sub>Ce<sub>0.8</sub>O<sub>1.9</sub> composite, *Electrochim. Acta* 252 (2017) 171–179.
- [37] J.H. Kim, M. Cassidy, J.T.S. Irvine, J. Bae, Advanced electrochemical properties of LnBa<sub>0.5</sub>Sr<sub>0.5</sub>Co<sub>2</sub>O<sub>5+δ</sub> (Ln=Pr, Sm, and Gd) as cathode materials for IT-SOFC, *J. Electrochem. Soc.* 156 (2009) B682–B689.
- [38] S. Choi, J. Shin, G. Kim, The electrochemical and thermodynamic characterization of PrBaCo<sub>2-x</sub>Fe<sub>x</sub>O<sub>5+δ</sub> (x=0, 0.5, 1) infiltrated into yttria-stabilized zirconia scaffold as cathodes for solid oxide fuel cells, *J. Power Sources* 201 (2012) 10–17.
- [39] B. Wei, Z. Lü, W. Pan, X. Huang, Y. Zhang, W. Su, Performance evaluation of an anode-supported solid oxide fuel cell with Ce<sub>0.8</sub>Sm<sub>0.2</sub>O<sub>1.9</sub> impregnated GdBaCo<sub>2</sub>O<sub>5+δ</sub> cathode, *Int. J. Hydrog. Energy* 37 (2012) 13491–13498.
- [40] Y. Chen, Y. Bu, B. Zhao, Y. Zhang, D. Ding, R. Hu, T. Wei, B. Rainwater, Y. Ding, F. Chen, C. Yang, J. Liu, M. Liu, A durable, high-performance hollow-nanofiber cathode for intermediate-temperature fuel cells, *Nano Energy* 26 (2016) 90–99.
- [41] J. Li, Q. Zhang, P. Qiu, L. Jia, B. Chi, J. Pu, J. Li, A CO<sub>2</sub>-tolerant, La<sub>2</sub>NiO<sub>4+δ</sub>-coated PrBa<sub>0.5</sub>Sr<sub>0.5</sub>Co<sub>1.5</sub>Fe<sub>0.5</sub>O<sub>5+δ</sub> cathode for intermediate temperature solid oxide fuel cells, *J. Power Sources* 342 (2017) 623–628.
- [42] R. Strandbakke, E. Vollestad, S.A. Robinson, M.-L. Fontaine, T. Norby, Ba<sub>0.5</sub>Gd<sub>0.8</sub>La<sub>0.7</sub>Co<sub>2</sub>O<sub>6-δ</sub> infiltrated in porous BaZr<sub>0.7</sub>Ce<sub>0.2</sub>Y<sub>0.1</sub>O<sub>3</sub> backbones as electrolyte material for proton ceramic electrolytes, *J. Electrochem. Soc.* 164 (2017) F196–F202.
- [43] Ld Santos-Gómez, J.M. Porras-Vázquez, E.R. Losilla, D. Marrero-López, Improving the efficiency of layered perovskite cathodes by microstructural optimization, *J. Mater. Chem. A* 5 (2017) 7896–7904.
- [44] Y. Chen, S. Yoo, W. Zhang, J.H. Kim, Y. Zhou, K. Pei, N. Kane, B. Zhao, R. Murphy, Y. Choi, M. Liu, Effective promotion of oxygen reduction reaction by in situ formation of nanostructured catalyst, *ACS Catal.* 9 (2019) 7137–7142.
- [45] L. Gui, Z. Wang, K. Zhang, B. He, Y. Liu, W. Zhou, J. Xu, Q. Wang, L. Zhao, Oxygen vacancies-rich Ce<sub>0.9</sub>Gd<sub>0.1</sub>O<sub>2-δ</sub> decorated Pr<sub>0.5</sub>Ba<sub>0.5</sub>CoO<sub>3-δ</sub> bifunctional catalyst for efficient and long-lasting rechargeable Zn-air batteries, *Appl. Catal. B Environ.* 266 (2020), 118656.
- [46] J.H. Kim, S. Yoo, R. Murphy, Y. Chen, Y. Ding, K. Pei, B. Zhao, G. Kim, Y. Choi, M. Liu, Promotion of oxygen reduction reaction on a double perovskite electrode by a water-induced surface modification, *Energy Environ. Sci.* 14 (2021) 1506–1516.
- [47] W. Zhang, Y. Zhou, A.M. Hussain, D. Song, Y. Miura, Y. Chen, Z. Luo, N. Kane, Y. Niu, N. Dale, Y. Fukuyama, M. Liu, High-performance, thermal cycling stable, coking-tolerant solid oxide fuel cells with nanostructured electrodes, *ACS Appl. Mater. Interfaces* 13 (2021) 4993–4999.
- [48] Z. Yue, L. Jiang, N. Ai, C. Guan, S.P. Jiang, X. Sun, W.D.A. Rickard, X. Wang, Y. Shao, K. Chen, Facile co-synthesis and utilization of ultrafine and highly active PrBa<sub>0.8</sub>Ca<sub>0.2</sub>Co<sub>2</sub>O<sub>5+δ</sub>-Gd<sub>0.2</sub>Ce<sub>0.8</sub>O<sub>1.9</sub> composite cathodes for solid oxide fuel cells, *Electrochim. Acta* 403 (2022), 139673, <https://doi.org/10.1016/j.electacta.2021.139673>.
- [49] Y. Zhou, E. Liu, Y. Chen, Y. Liu, L. Zhang, W. Zhang, Z. Luo, N. Kane, B. Zhao, L. Soule, Y. Niu, Y. Ding, H. Ding, D. Ding, M. Liu, An active and robust air electrode for reversible protonic ceramic electrochemical cells, *ACS Energy Lett.* 6 (2021) 1511–1520.
- [50] S.P. Jiang, Nanoscale and nano-structured electrodes of solid oxide fuel cells by infiltration: advances and challenges, *Int. J. Hydrog. Energy* 37 (2012) 449–470.
- [51] Z.Y. Jiang, C.R. Xia, F.L. Chen, Nano-structured composite cathodes for intermediate-temperature solid oxide fuel cells via an infiltration/impregnation technique, *Electrochim. Acta* 55 (2010) 3595–3605.
- [52] W. Kobsiriphat, B.D. Madsen, Y. Wang, L.D. Marks, S.A. Barnett, La<sub>0.8</sub>Sr<sub>0.2</sub>Cr<sub>1-x</sub>Ru<sub>x</sub>O<sub>3-δ</sub>-Gd<sub>0.1</sub>Ce<sub>0.9</sub>O<sub>1.95</sub> solid oxide fuel cell anodes: Ru precipitation and electrochemical performance, *Solid State Ion.* 180 (2009) 257–264.
- [53] C. Yang, Z. Yang, C. Jin, G. Xiao, F. Chen, M. Han, Sulfur-tolerant redox-reversible anode material for direct hydrocarbon solid oxide fuel cells, *Adv. Mater.* 24 (2012) 1439–1443.



- [54] D. Neagu, G. Tsekouras, D.N. Miller, H. Ménard, J.T.S. Irvine, In situ growth of nanoparticles through control of non-stoichiometry, *Nat. Chem.* 5 (2013) 916–923.
- [55] J.-H. Myung, D. Neagu, D.N. Miller, J.T.S. Irvine, Switching on electrocatalytic activity in solid oxide cells, *Nature* 537 (2016) 528–531.
- [56] Z. Du, H. Zhao, S. Yi, Q. Xia, Y. Gong, Y. Zhang, X. Cheng, Y. Li, L. Gu, K. Świerczek, High-performance anode material  $\text{Sr}_2\text{FeMo}_{0.65}\text{Ni}_{0.35}\text{O}_{6-\delta}$  with in situ exsolved nanoparticle catalyst, *ACS Nano* 10 (2016) 8660–8669.
- [57] L. Ye, M. Zhang, P. Huang, G. Guo, M. Hong, C. Li, J.T. Irvine, K. Xie, Enhancing  $\text{CO}_2$  electrolysis through synergistic control of non-stoichiometry and doping to tune cathode surface structures, *Nat. Commun.* 8 (2017) 14785.
- [58] Y.-F. Sun, Y.-Q. Zhang, J. Chen, J.-H. Li, Y.-T. Zhu, Y.-M. Zeng, B.S. Amirkhiz, J. Li, B. Hua, J.-L. Luo, New opportunity for in situ exsolution of metallic nanoparticles on perovskite parent, *Nano Lett.* 16 (2016) 5303–5309.
- [59] G. Yang, W. Zhou, M. Liu, Z. Shao, Enhancing electrode performance by exsolved nanoparticles: a superior cobalt-free perovskite electrocatalyst for solid oxide fuel cells, *ACS Appl. Mater. Interfaces* 8 (2016) 35308–35314.
- [60] Z. Xu, Y. Li, Y. Wan, S. Zhang, C. Xia, Nickel enriched Ruddlesden-Popper type lanthanum strontium manganite as electrode for symmetrical solid oxide fuel cell, *J. Power Sources* 425 (2019) 153–161.
- [61] D. Neagu, T.-S. Oh, D.N. Miller, H. Menard, S.M. Bukhari, S.R. Gamble, R.J. Gorte, J.M. Vohs, J.T.S. Irvine, Nano-socketed nickel particles with enhanced coking resistance grown in situ by redox exsolution, *Nat. Commun.* 6 (2015) 8120.
- [62] N. Ai, Y. Zou, Z. Chen, K. Chen, S.P. Jiang, Progress on direct assembly approach for in situ fabrication of electrodes of reversible solid oxide cells, *Mater. Rep. Energy* 1 (2021), 100023.
- [63] K. Chen, N. Li, N. Ai, M. Li, Y. Cheng, W.D.A. Rickard, J. Li, S.P. Jiang, Direct application of cobaltite-based perovskite cathodes on the yttria-stabilized zirconia electrolyte for intermediate temperature solid oxide fuel cells, *J. Mater. Chem. A* 4 (2016) 17678–17685.
- [64] N. Ai, N. Li, S. He, Y. Cheng, M. Saunders, K. Chen, T. Zhang, S.P. Jiang, Highly active and stable  $\text{Er}_{0.4}\text{Bi}_{1.6}\text{O}_3$  decorated  $\text{La}_{0.76}\text{Sr}_{0.19}\text{MnO}_{3+\delta}$  nanostructured oxygen electrodes for reversible solid oxide cells, *J. Mater. Chem. A* 5 (2017) 12149–12157.
- [65] N. Ai, M. Chen, S. He, K. Chen, T. Zhang, S.P. Jiang, High performance nanostructured bismuth oxide-cobaltite as a durable oxygen electrode for reversible solid oxide cells, *J. Mater. Chem. A* 6 (2018) 6510–6520.
- [66] S. He, K. Chen, M. Saunders, Z. Quadir, S. Tao, J.T.S. Irvine, C.Q. Cui, S.P. Jiang, Interface formation and Mn segregation of directly assembled  $\text{La}_{0.8}\text{Sr}_{0.2}\text{MnO}_3$  cathode on  $\text{Y}_2\text{O}_3\text{-ZrO}_2$  and  $\text{Gd}_2\text{O}_3\text{-CeO}_2$  electrolytes of solid oxide fuel cells, *Solid State Ion.* 325 (2018) 176–188.
- [67] S. He, M. Saunders, K. Chen, H. Gao, A. Suvorova, W.D.A. Rickard, Z. Quadir, C. Q. Cui, S.P. Jiang, A FIB-STEM study of strontium segregation and interface formation of directly assembled  $\text{La}_{0.6}\text{Sr}_{0.4}\text{Co}_{0.2}\text{Fe}_{0.8}\text{O}_{3-\delta}$  cathode on  $\text{Y}_2\text{O}_3\text{-ZrO}_2$  electrolyte of solid oxide fuel cells, *J. Electrochem. Soc.* 165 (2018) F417–F429.
- [68] Z. Chen, W. Jiang, Z. Lu, Z. Wang, Z. Chen, S.P. Jiang, T. Lin, Y. Shao, D. Tang, K. Chen, N. Ai, Accelerating effect of polarization on electrode/electrolyte interface generation and electrocatalytic performance of  $\text{Er}_{0.4}\text{Bi}_{1.6}\text{O}_3$  decorated  $\text{Sm}_{0.95}\text{CoO}_{3-\delta}$  cathodes, *J. Power Sources* 465 (2020), 228281.
- [69] K. Chen, Z. Lü, N. Ai, X. Huang, Y. Zhang, X. Ge, X. Xin, X. Chen, W. Su, Fabrication and performance of anode-supported YSZ films by slurry spin coating, *Solid State Ion.* 177 (2007) 3455–3460.
- [70] K. Chen, X. Chen, Z. Lü, N. Ai, X. Huang, W. Su, Performance of an anode-supported SOFC with anode functional layers, *Electrochim. Acta* 53 (2008) 7825–7830.
- [71] J.T.S. Irvine, D. Neagu, M.C. Verbraeken, C. Chatzichristodoulou, C. Graves, M. B. Mogensen, Evolution of the electrochemical interface in high-temperature fuel cells and electrolyzers, *Nat. Energy* 1 (2016) 15014.
- [72] Y. Chen, S. Yoo, Y. Choi, J.H. Kim, Y. Ding, K. Pei, R. Murphy, Y. Zhang, B. Zhao, W. Zhang, H. Chen, Y. Chen, W. Yuan, C. Yang, M. Liu, A highly active,  $\text{CO}_2$ -tolerant electrode for the oxygen reduction reaction, *Energy Environ. Sci.* 11 (2018) 2458–2466.
- [73] Y. Zhang, C. Xia, A particle-layer model for solid-oxide-full-cell cathodes with different structures, *J. Power Sources* 195 (2010) 4206–4212.
- [74] Y. Zhang, F. Yan, M. Yan, Y. Wan, Z. Jiao, C. Xia, F. Chen, M. Ni, High-throughput, super-resolution 3D reconstruction of nano-structured solid oxide fuel cell electrodes and quantification of microstructure-property relationships, *J. Power Sources* 427 (2019) 112–119.
- [75] K. Chen, N. Li, N. Ai, Y. Cheng, W.D.A. Rickard, S.P. Jiang, Polarization-induced interface and Sr segregation of in situ assembled  $\text{La}_{0.6}\text{Sr}_{0.4}\text{Co}_{0.2}\text{Fe}_{0.8}\text{O}_{3-\delta}$  electrodes on  $\text{Y}_2\text{O}_3\text{-ZrO}_2$  electrolyte of solid oxide fuel cells, *ACS Appl. Mater. Interfaces* 8 (2016) 31729–31737.
- [76] K. Chen, S. He, N. Li, Y. Cheng, N. Ai, M. Chen, W.D.A. Rickard, T. Zhang, S. P. Jiang, Nb and Pd co-doped  $\text{La}_{0.57}\text{Sr}_{0.38}\text{Co}_{0.19}\text{Fe}_{0.665}\text{Nb}_{0.095}\text{Pd}_{0.05}\text{O}_{3-\delta}$  as a stable, high performance electrode for barrier-layer-free  $\text{Y}_2\text{O}_3\text{-ZrO}_2$  electrolyte of solid oxide fuel cells, *J. Power Sources* 378 (2018) 433–442.